

# Characterization of Bacterial Magnetic Nanostructures Using High-Resolution Transmission Electron Microscopy and Off-Axis Electron Holography

Mihály Pósfai<sup>1</sup> (✉) · Takeshi Kasama<sup>2,3</sup> · Rafal E. Dunin-Borkowski<sup>2,3</sup>

<sup>1</sup>Department of Earth and Environmental Sciences, Pannon University, POB 158,  
8200 Veszprém, Hungary  
posfaim@almos.vein.hu

<sup>2</sup>Frontier Research System, The Institute of Physical and Chemical Research, Hatoyama,  
350-0395 Saitama, Japan

<sup>3</sup>Department of Materials Science and Metallurgy, University of Cambridge,  
Pembroke Street, Cambridge CB2 3QZ, UK

<b>1</b>	<b>Introduction</b>	198
<b>2</b>	<b>Techniques</b>	198
2.1	High-Resolution Transmission Electron Microscopy	198
2.2	Off-Axis Electron Holography	199
2.3	Electron Tomography	200
<b>3</b>	<b>The Structures and Magnetic Properties of Magnetite Magnetosomes</b>	200
3.1	Cubooctahedral Magnetite Crystals	202
3.2	Elongated Prismatic Magnetite Crystals	207
3.3	Unusually Large Magnetite Magnetosomes, and Scattered or Clustered Crystals	211
<b>4</b>	<b>The Crystal Structures and Magnetic Properties of Iron Sulfide Magnetosomes</b>	213
<b>5</b>	<b>Quantitative Measurements Using Electron Holography</b>	217
<b>6</b>	<b>Summary</b>	219
	<b>References</b>	222

**Abstract** Magnetotactic bacteria can be regarded as model systems for studying the structural, chemical, and magnetic properties of arrangements of ferrimagnetic iron oxide and sulfide nanocrystals. The aim of the present chapter is to show how the size, shape, crystal structure, crystallographic orientation, and spatial arrangement of bacterial magnetite ( $\text{Fe}_3\text{O}_4$ ) and greigite ( $\text{Fe}_3\text{S}_4$ ) crystals affect their magnetic properties. We present recent results obtained using transmission electron microscopy (TEM) techniques, including high-resolution TEM imaging and off-axis electron holography.

## 1

### Introduction

Magnetotactic bacteria contain intracellular ferrimagnetic crystals that are typically 30–120 nm in size and are arranged in a linear chain configuration. The magnetic properties of the bacterial iron oxide and sulfide nanocrystals depend on several factors, including crystal structure and habit, the direction of the crystal's elongation, and the orientation and spacing of each crystal with respect to its neighbors. It is necessary to study these properties in order to obtain an insight into the magnetic behavior of such magnetic particles.

The transmission electron microscope is a powerful tool for characterizing the physical and chemical properties of materials at high spatial resolution, and has been used for the study of bacterial magnetosomes since the discovery of magnetotactic bacteria (Blakemore 1975). Advanced transmission electron microscopy (TEM) techniques, including off-axis electron holography (EH) (Tonomura 1992; Völkl et al. 1998) and electron tomography (ET), for applications in the physical sciences (Midgley et al. 2001) have become widely available in the past decade. The combination of these new techniques and conventional high-resolution TEM (HRTEM) and selected-area electron diffraction (SAED) now allows the relationships between the structures, three-dimensional morphologies, configurations, and magnetic properties of magnetosomes to be studied in detail.

In this chapter, we briefly describe the principles of HRTEM, EH, and ET. The structural and magnetic properties of magnetite and sulfide magnetosomes are then discussed, with an emphasis on the interpretation of recent EH results. The quantitative nature of EH is highlighted.

## 2

### Techniques

#### 2.1

##### High-Resolution Transmission Electron Microscopy

In HRTEM, an image is formed by using a large objective aperture to cause one or more beams that have been diffracted by a specimen to interfere with the transmitted beam. In modern generations of transmission electron microscopes, the image resolution is better than 0.2 nm, and individual atomic columns can be resolved in many crystalline inorganic materials. If the objective lens defocus and image astigmatism and incident beam alignment are optimized, then the resulting image can be interpreted directly in terms of the projected crystal potential. With care, crystal lattice spacings, angles between lattice planes, and defects can be identified from such images. As the elec-

tron dose used to acquire a single image is typically approximately 500–2000 electrons per square angstrom, it is not usually possible to examine organic materials directly under such intense imaging conditions.

## 2.2

### Off-Axis Electron Holography

EH allows the phase shift of a high-energy electron wave that has passed through a specimen to be recovered. The phase shift is, in turn, sensitive to the in-plane component of the magnetic induction and the electrostatic potential in the specimen. The TEM mode of off-axis EH is illustrated schematically in the form of a ray diagram in Fig. 1. The specimen is examined using highly coherent illumination from a field-emission gun electron source, with the region of interest positioned so that it covers approximately half the field of view. A (typically positive) voltage is applied to an electron biprism, which is located close to a conjugate image plane in the microscope, to overlap the electron wave that has passed through a vacuum (or through a thin region of support film) with a part of the same electron wave that has passed through the region of interest on the specimen, to form a hologram in a slightly defocused image plane. When magnetic materials are examined, holograms are normally recorded with the conventional microscope objective lens turned off, as its strong magnetic field would saturate the magnetization in the specimen in the electron beam direction. A Lorentz lens (a high-strength minilens located below the lower objective pole piece) can then be used to record

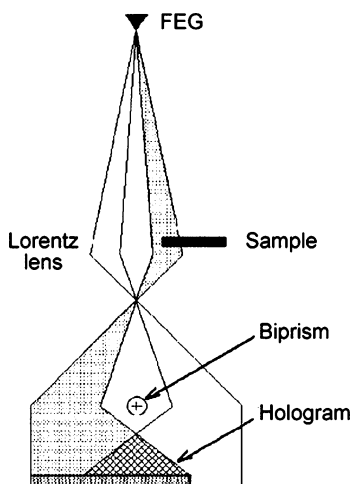


**Fig. 1** Ray diagram illustrating the components of a transmission electron microscope that are required for off-axis electron holography (EH) of nanoscale magnetic materials. See text for details. FEG field-emission gun

holograms at high magnification with the specimen in a magnetic-field-free environment. The objective lens can also be excited slightly and the specimen tilted to apply known magnetic fields to follow magnetization processes in situ in the transmission electron microscope. When magnetic nanostructures are examined, the magnetic contribution to the phase shift recorded from a hologram must usually be separated from the dominant mean inner potential (MIP) contribution. This separation can be achieved by recording two holograms that differ only in the (opposite) directions of magnetization in the specimen. The magnetic contribution is then calculated by taking half of the difference between the phases of the holograms (Dunin-Borkowski et al. 2004). All of the magnetic induction maps presented in this chapter show the ferrimagnetic crystals in their remanent state, since the holograms were recorded in zero magnetic field.

### 2.3

#### **Electron Tomography**

In the life sciences, ET has been used to image complex nanoscale structures in three dimensions since the late 1960s (DeRosier and Klug 1968). In general, tomography requires a series of images (projections) of an object to be recorded at successive specimen tilt angles, using a signal that is related monotonically to the projected specimen thickness. Bright-field images, in which mass-thickness contrast dominates, are suitable for applications in the life sciences. However, in the physical sciences, crystalline objects result in the presence of diffraction and Fresnel contrast, and an incoherent form of imaging is more suitable. Images are then typically recorded using high-angle annular dark-field imaging using a scanned probe or energy-filtered transmission electron microscope. As many images as possible are recorded over as large a range of tilt angles as possible. After acquisition of the tilt series, each image is back-projected along the original tilt angle. The overlap of all projections then leads to a reconstruction of the three-dimensional object. Artifacts are minimized by employing an iterative routine that constrains the final reconstruction to match the original projections (Frank 1992).

## 3

### **The Structures and Magnetic Properties of Magnetite Magnetosomes**

The structures and morphologies of magnetite magnetosomes have been studied since the discovery of magnetotactic bacteria (Balkwill et al. 1980; Towe and Moench 1981; Matsuda et al. 1983). Most studies found essentially no defects in the magnetite crystals (Mann et al. 1984; Sparks et al.

1990; Meldrum et al. 1993a, b). More structural disorder, primarily spinel-type twinning, was reported subsequently (Devouard et al. 1998), whereas other defects, which were interpreted as screw dislocations, were described in magnetite from uncultured magnetotactic bacteria (Taylor et al. 2001). Nevertheless, most bacterial magnetite crystals are free of extended structural defects.

The crystal habits of magnetite magnetosomes are species-specific, and have been described in terms of categories that include cubooctahedral, prismatic and arrowhead-shaped (Mann et al. 1984; Vali and Kirschvink 1990; Bazylinski and Frankel 2004). The sizes and shapes of magnetite crystals were found to be affected only slightly by variations in culturing conditions (Meldrum et al. 1993a, b). When they are elongated, bacterial magnetite crystals typically have elongation directions that are parallel to [111] (Mann et al. 1984; Sparks et al. 1990; Lins et al. 2005); however, highly elongated magnetite magnetosomes with elongation directions that are parallel to [112] (Mann et al. 1987; Taylor et al. 2001), [100] (Iida and Akai 1996; Taylor et al. 2001; Kasama et al. 2006a; Pósfai et al. 2006), and [110] (Taylor and Barry 2004) have also been described.

The magnetic dipole moments of magnetosome chains were calculated by Frankel (1984). On the basis of their sizes, the individual magnetosomes were assumed to be single magnetic domains. If the individual moments were assumed to be aligned parallel to each other and to the chain direction, then an ordered magnetite chain was calculated to have an overall magnetic dipole moment approximately equal to the sum of the individual magnetosome magnetic moments. Rock magnetism measurements of intact cells and separated chains were in agreement with these calculations, and indicated that both the dominant single-domain character and the chain configuration of the magnetite particles could be detected using bulk magnetic methods (Moskowitz et al. 1989, 1993; Weiss et al. 2004). Magnetic force microscopy was used to measure the magnetic dipole moment of a single cell (Proksch et al. 1995). Because of its high spatial resolution and sensitivity, EH takes the study of the magnetic properties of bacterial magnetosomes forward significantly, as described later.

Since crystal shape is important for determining the magnetic behavior of nanocrystals, it is convenient to describe the structural and magnetic characteristics of magnetite magnetosomes according to the three morphological groups that we have already described. The structures of all three types of crystals have been studied using HRTEM and SAED, and the magnetic microstructures of cubooctahedral and prismatic magnetosomes have been studied using EH. In the following sections, we discuss the structural and magnetic properties of cubooctahedral and prismatic magnetite magnetosomes. EH studies of arrowhead-shaped crystals, which are in progress, will be described elsewhere.

### 3.1

#### Cubooctahedral Magnetite Crystals

Magnetotactic spirilla such as *Magnetospirillum magnetotacticum* and *Magnetospirillum gryphiswaldense* produce magnetite crystals that are usually termed cubooctahedral magnetite (Bazylinski and Frankel 2000). Their morphologies, which are approximately equidimensional, can be described most simply in terms of a combination of the  $\{111\}$  and  $\{100\}$  forms (the octahedron and the cube, respectively). Some bacterial strains contain magnetite crystals that appear to be almost perfect octahedra, whereas other strains produce nanocrystals that are combinations of the octahedron, the cube, and the dodecahedron  $\{110\}$  (Devouard et al. 1998; Arató et al. 2005). For simplicity, all of these variations of roughly equidimensional magnetite morphologies are referred to here by the term cubooctahedral.

The precise identification of all of the faces of a nanocrystal is not straightforward, and has only been carried out in a few cases. As discussed by Buseck et al. (2001), the projected outlines of magnetosomes in bright-field TEM images provide ambiguous information about their three-dimensional shapes. In particular, it is difficult to identify whether a straight segment of the crystal outline is a projection of a face that is parallel to the electron beam or that of an edge shared by two faces (Lins et al. 2005). This difficulty is exacerbated by the fact that some parts of a crystal outline may appear rounded or rough. In addition, the details of such contrast features may vary with objective lens defocus. The ambiguity of crystal shape determination from two-dimensional projections was illustrated by a debate on the potential biogenic origin of magnetite crystals in the Martian meteorite ALH84001 (Thomas-Kepřta et al. 2000; Buseck et al. 2001; Clemett et al. 2002; Golden et al. 2004), the central issue of which was whether the bacterial magnetite crystals have unique morphological characteristics that distinguish them from crystals that formed inorganically.

Since the contrast in HRTEM images is sensitive to the thickness of a crystal, it is possible to obtain some information about the three-dimensional crystal morphology by observing the contrast variation in experimental images. Careful examination of the HRTEM image of a magnetite magnetosome in Fig. 2a reveals that the contrast shows a characteristic variation from the edges to the center of the crystal. Regions having different contrast are marked by different shades of gray in Fig. 2b, with each shade representing regions of similar crystal thickness projected in the direction of the electron beam. Although care is required with the interpretation of such images because the exit surface of the crystal also varies, the crystal appears to be much thinner at regions marked A than at those marked B, even though both regions are near the outline of the crystal's projected image. These observations suggest that the surfaces that are parallel to  $(01\bar{1})$  and  $(0\bar{1}1)$  planes are faces that are aligned parallel to the incident electron beam, whereas at the points

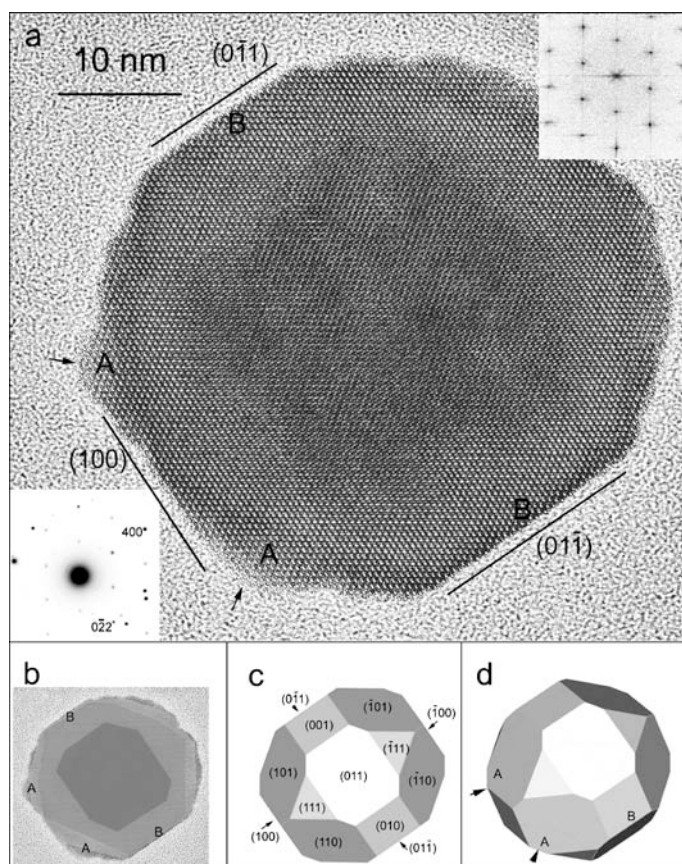


**Fig. 2** **a** High-resolution transmission electron microscopy (HRTEM) image of a structurally perfect cubooctahedral magnetite crystal from *Magnetospirillum gryphiswaldense*, viewed along [011]. The insets in the lower-left corner and the upper-right corner are an experimental selected-area electron diffraction (SAED) pattern and a Fourier transform of the image, respectively. The labels A and B and the short arrows are discussed in the text. **b** "Thickness map" of the magnetosome in **a**, inferred from the variations in the HRTEM image contrast. **c**, **d** Assumed morphological model for the magnetite crystal in **a**, displayed in two slightly different orientations

that are marked by short arrows in Fig. 2a several edges meet, resulting in regions that are thinner in projection. A possible morphological model for this cubooctahedral magnetite crystal is presented in Fig. 2c. In order to illustrate the crystal morphologies at the regions marked A and B, the same model is shown from a slightly different direction in Fig. 2d.

Another example of the determination of crystal thickness from an HRTEM image is shown in Fig. 3. This small magnetite magnetosome is from a cell of a mutant of *Magnetospirillum gryphiswaldense* that synthesizes

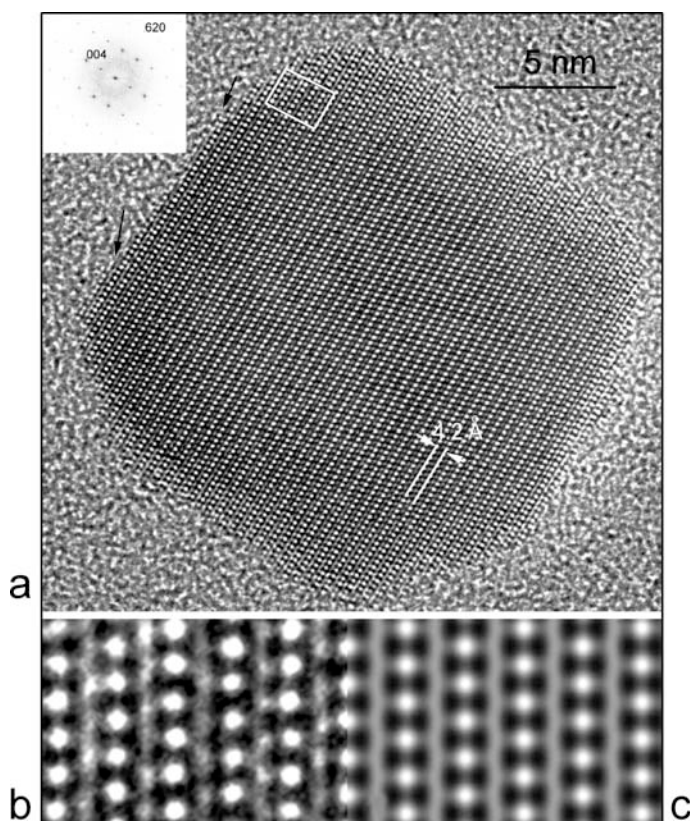


**Fig. 3** **a** HRTEM image and Fourier transform (*inset*) of a magnetite magnetosome from a mutant of *Magnetospirillum gryphiswaldense*, viewed along [1–30]. **b** A magnified image of the boxed region in **a**. **c** Calculated HRTEM image, simulated using the parameters 400-kV accelerating voltage,  $C_s = 1$  mm,  $-74$ -nm objective lens defocus,  $6\text{-nm}^{-1}$  objective aperture, 4-nm crystal thickness, no crystal or beam tilt. The *arrows* in **a** mark terminating structural planes on the crystal surface

slightly smaller magnetosome crystals. By comparing the contrast in experimental and simulated HRTEM images, the approximate thickness of the crystal can be determined. The boxed region in Fig. 3a is shown enlarged in Fig. 3b, and a corresponding calculated image is shown in Fig. 3c. Although it is notoriously difficult to match calculated HRTEM images reliably to experimental images, the simulated and experimental images in Fig. 3 show a good match of contrast, suggesting that the thickness value (4 nm) that was used for the calculation is approximately correct. The contrast varies little from the edge to the center of the particle, suggesting that this magnetosome is very thin and may have a tabular morphology. On the edge of the crystal, terminating structural planes (arrowed in Fig. 3a) appear to be edge-on views of atomic-scale steps on the surface of the crystal.



Cubo-octahedral magnetite magnetosomes typically do not contain extended defects other than twin boundaries (Fig. 4). Twins are of spinel type, as also observed in inorganically formed magnetite. Spinel twins are related to each other by a twofold axis that is parallel to  $[111]$ . The twin boundary can lie along a single  $(111)$  plane, although in many bacterial magnetite crystals

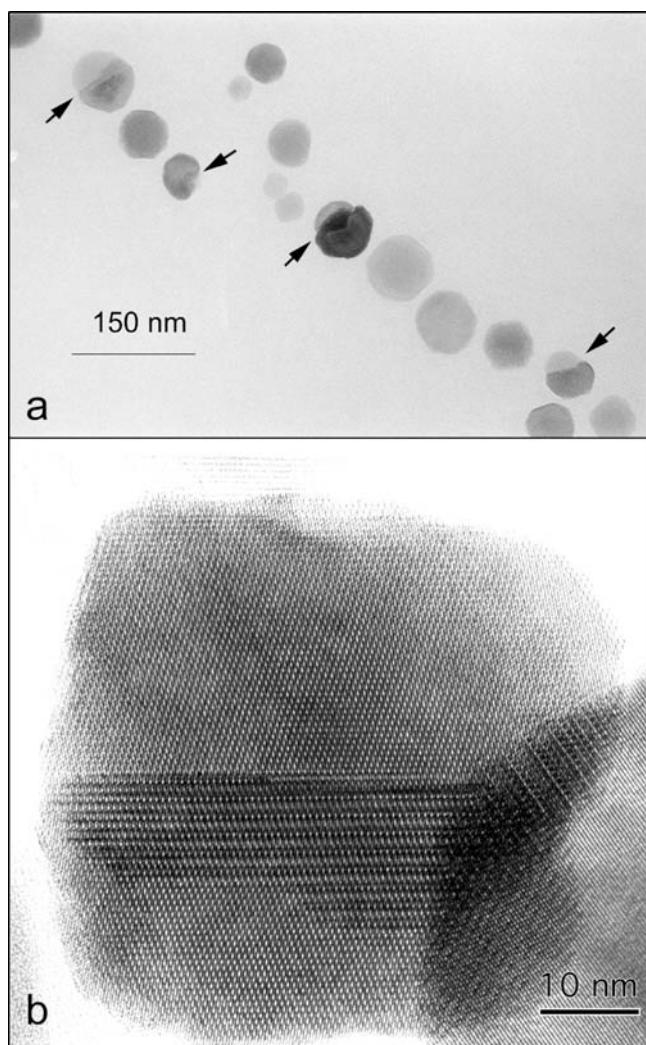


**Fig. 4** **a** Bright-field TEM image of a chain fragment of magnetite magnetosomes from *Magnetospirillum gryphiswaldense* (wild-type), showing twinned crystals (arrowed). **b** HRTEM image of a twinned magnetite crystal from *Magnetospirillum magnetotacticum* strain MS-1. The two twin member crystals overlap, producing a Moiré effect. (**b** From Devouard et al. 1998)

the two parts of the twin meet at an irregular surface (Fig. 4b). The proportion of twinned magnetosomes is strain-specific (Devouard et al. 1998). Whereas in some strains fewer than 1% of all magnetite crystals are twinned, a strain containing a large proportion (approximately 70%) of twinned crystals has also been observed (D. Bazylinski, private communication). With rare exceptions, twin boundaries occur perpendicular to the chain axis; thus, they are not expected to affect the direction of the magnetic induction within the magnetosomes significantly, as the magnetocrystalline easy axis of magnetite is [111] (Dunlop and Özdemir 1997). Multiple twin boundaries tend to be more irregular and are less likely to be perpendicular to the chain axis; however, the proportion of such boundaries is too small to have a significant effect on the magnetic induction of the chain.

Although the relative orientations of cubooctahedral magnetite crystals within chains have not been studied in detail, the general direction of the chain axis appears to coincide with [111] for most crystals. Scheffel et al. (2005) found that in *Magnetospirillum gryphiswaldense* the magnetosomes are attached to an organic filamentous structure that runs along the long axis of the cell. In this study, an acidic protein was shown to anchor the magnetosomes to the filament. This protein appears to be responsible for setting [111] in each crystal to be parallel to the chain axis (see also Komeili, this volume).

The magnetic induction in chains of cubooctahedral magnetite crystals has been studied in *Magnetospirillum magnetotacticum* strain MS-1 using EH (Dunin-Borkowski et al. 1998, 2001). Figure 5 shows a magnetic induction map obtained from EH images of a magnetosome chain that can be regarded as representative for MS-1. The magnetite crystals are about 45 nm in size. The direction of the magnetic phase contours shown in Fig. 5 represents the direction of the local magnetic induction (projected in the electron beam direction), and the density of the contour lines provides a measure of the strength of the local in-plane induction. The same amount of magnetic flux is enclosed between any two adjacent contours.

In Fig. 5, the crystal size along the chain is not uniform. The sizes of the magnetosomes gradually decrease on the right side of the chain, whereas the corresponding change on the left side of the chain is more abrupt. This variation in crystal size affects the strength of the local magnetic induction. The contour map shows a larger number of closely spaced contours at the left end of the chain, where larger crystals are present. The crystals at the right end of the chain are below approximately 20 nm in size, and thus would be expected to be superparamagnetic if they were isolated. However, the direction of the magnetic contours is confined to be parallel to the chain axis in these crystals, indicating that they are stable single magnetic domains at room temperature. This behavior likely results from magnetic interactions between adjacent nanocrystals in the linear chain configuration.

Two smaller crystals are present at the position marked by the white arrow in Fig. 5, creating a defect in the chain structure and resulting in slightly

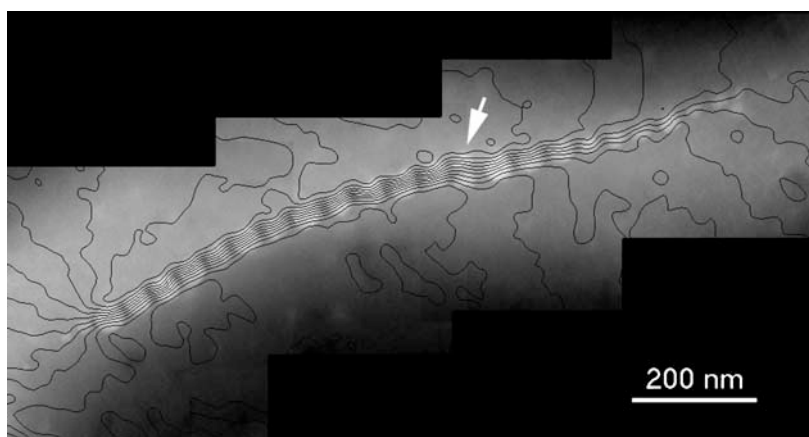


**Fig. 5** Magnetic induction map recorded using EH from a chain of magnetite magnetosomes in a cell of *Magnetospirillum magnetotacticum* strain MS-1. The mean inner potential contribution to the phase shift was removed from the measured signal before creating the contour map. The *white arrow* marks a defect in the chain that consists of two small crystals. The spacing of the contours is 0.064 rad. (From Dunin-Borkowski et al. 1998, 2001)

poorer confinement of the magnetic phase contours. In a similar cell, slight waviness of the contour lines was caused by a small displacement of the magnetosomes from the axis of the magnetosome chain (Dunin-Borkowski et al. 1998, 2001). The contour lines within these magnetosomes were observed to bend to follow the positions of the crystals, irrespective of their crystallographic orientations. Thus, the positions of the magnetite crystals dictate the local direction of the magnetic induction. Since the crystals are roughly equidimensional, neither shape nor magnetocrystalline anisotropy has a significant effect on the magnetic induction for chains of cubooctahedral magnetite magnetosomes.

### 3.2

#### **Elongated Prismatic Magnetite Crystals**

Magnetite magnetosomes with elongated “prismatic” habits typically occur in magnetotactic vibrios and cocci, collected from both freshwater and marine environments. In many types of cells, these crystals form well-organized single or double chains. Twinning occurs in prismatic magnetite magnetosomes (Devouard et al. 1998), but other types of structural defect have not been observed.

The magnetite crystals from a single cell of a freshwater magnetotactic coccus that are shown in Fig. 6a and b are free of extended defects. Each of the numbered crystals in the double chain shown in Fig. 6a was aligned to either

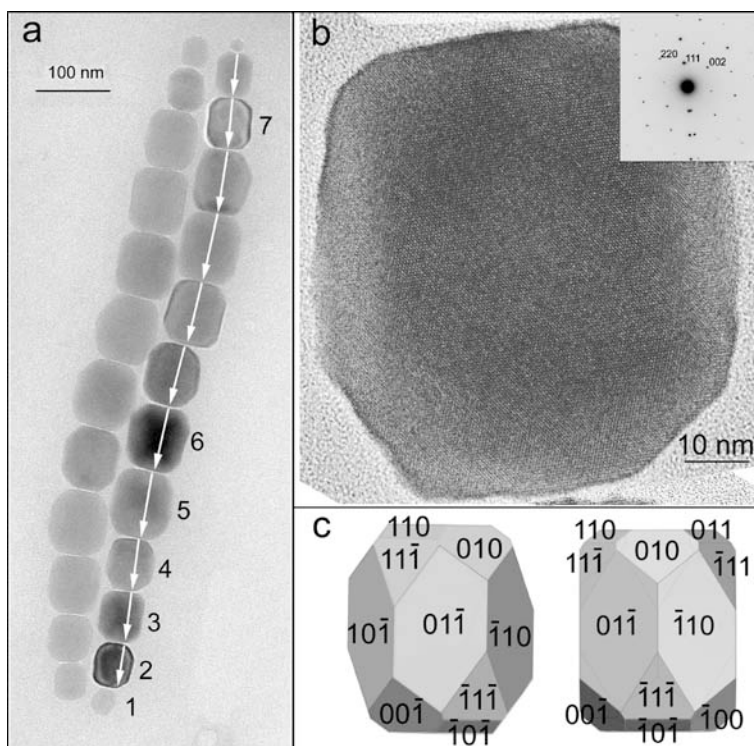


**Fig. 6** **a** Bright-field TEM image of a double chain of magnetite magnetosomes from a single cell of a freshwater magnetotactic coccus. The numbered crystals were found to have their  $[111]$  directions parallel to the magnetosome chain axis to within  $3^\circ$  (except for crystal 1 at the end of the chain, which was misaligned with respect to the chain axis). **b** HRTEM image and SAED pattern of crystal 4 from **a**, viewed along  $[-110]$ . **c** Model for the assumed morphology of the magnetite crystals in **a**, shown in the two directions  $[011]$  and  $[121]$  in which HRTEM images were recorded. (**a**, **b** From Simpson et al. 2005)

a  $[110]$  or a  $[112]$  axis, in order to determine the relative orientations of the crystals with respect to one another (Simpson et al. 2005). Significantly, the  $[111]$  axes of almost all of the crystals were found to be aligned parallel to the chain axis to within a few degrees, whereas their crystallographic directions perpendicular to the chain axis were random. Similar arrangements were found in other cells that contained single chains of magnetite magnetosomes with prismatic habits (Lins et al. 2005; I. Dódy, private communication). Assuming that the relative orientations of the crystals are not affected by air-drying of the cells on TEM grids, these results suggest that biological control of the orientations of magnetosomes is stricter in setting the  $[111]$  magnetic easy axis to be parallel to the chain axis than in controlling the orientations of the crystals perpendicular to this direction.

A tentative model for the typical morphology of the magnetosomes shown in Fig. 6a is illustrated for two orientations of the crystal in Fig. 6c. The inferred morphology is formed from a combination of the  $\{111\}$ ,  $\{110\}$ , and  $\{100\}$  forms. Characteristically for prismatic magnetite magnetosomes, the largest faces are those six faces of  $\{110\}$  that are parallel to the  $[111]$  axis of elongation.

A magnetic induction map obtained from the double magnetite chain shown in Fig. 6a using EH is presented in Fig. 7. In each crystal, the direction of the recorded magnetic induction is parallel to the direction of elongation of the crystal. Since this direction coincides with  $[111]$  and the chain axis, the effects of shape and magnetocrystalline anisotropy and interactions between neighboring crystals reinforce each other. In other chains of prismatic magnetite magnetosomes, magnetic phase contours have also been found to be parallel to the elongation axes of the individual crystals (Figs. 8, 9). As a consequence of the precise alignment of the elongation axes of the magnetosomes with the chain axis, as well as the proximity of adjacent crystals, the magnetic phase contours are highly parallel to each other and confined within the magnetosomes. In Fig. 9, the two chains within a single cell show little magnetic interaction with each other and appear to be largely magnetically independent. In contrast, the double chain shown in Figs. 6 and 7 can be regarded as similar to a single bar magnet, with the magnetic flux returning outside the combined double chain.

One of the most studied magnetotactic strains is MV-1. Cells of this strain also contain elongated, prismatic magnetite crystals that form a single chain in each cell (Fig. 8). Each magnetosome is a single magnetic domain. However, the gaps between the magnetosomes are larger than in the double chain shown in Figs. 6 and 7. As a result, the separation of the magnetic contour

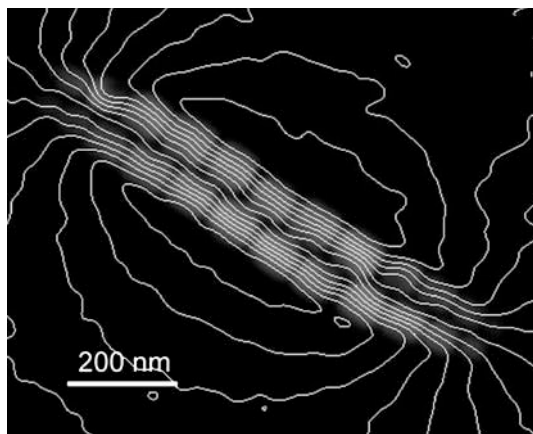


**Fig. 7** Magnetic induction map recorded using EH from the double chain of magnetite magnetosomes shown in Fig. 6a. The spacing of the contours is 0.3 rad

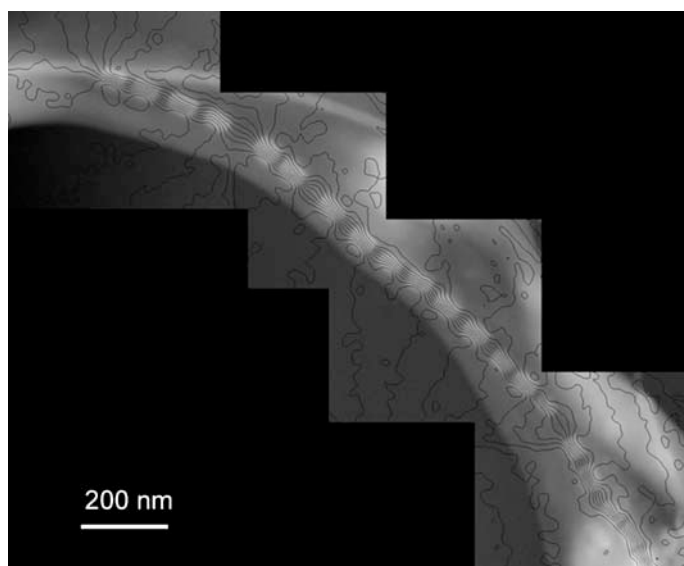


**Fig. 8** Magnetic induction map recorded using EH from a magnetite magnetosome chain from bacterial strain MV-1. The phase contour spacing is 0.064 rad. (From Dunin-Borkowski et al. 1998, 2001)

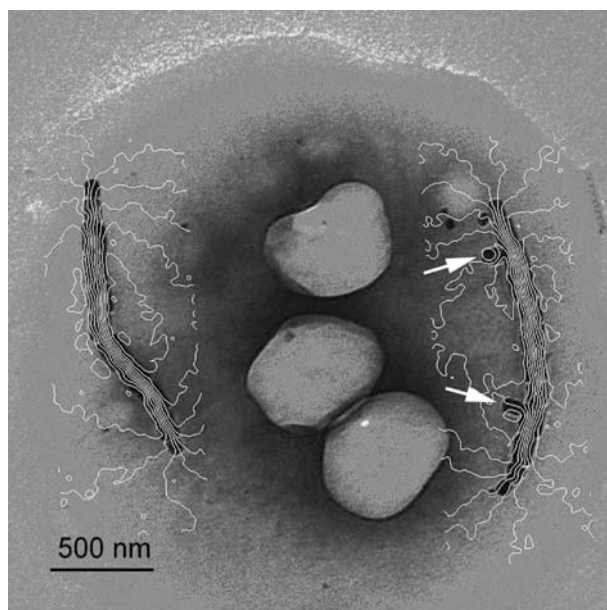


**Fig. 9** Magnetic induction map recorded using EH from two single chains of magnetite crystals in a cell of a magnetotactic coccus. In the right chain, the two *arrowed* magnetosomes are away from the primary chain axis, with their axis of elongation perpendicular to the chain. (From Dunin-Borkowski et al. 2004)

lines increases in the gaps between the crystals. Even if a crystal is misplaced from the chain axis (for example, the fourth magnetosome from the left in Fig. 8), the direction of the contour lines inside the crystal is parallel to its elongation axis, suggesting that shape anisotropy plays a dominant role in the elongated magnetite crystals in MV-1.

In the cell shown in Fig. 9, two single chains of prismatic magnetite magnetosomes are positioned at opposite sides of the cell. Hanzlik et al. (1996) suggested that such chain arrangements may balance such a cell magnetically as it swims parallel to the direction of an external magnetic field. A noteworthy feature of the magnetosome chain on the right of Fig. 9 is that two magnetite crystals are in irregular positions perpendicular to the chain axis. The fact that the magnetic phase contours inside these two magnetosomes remain parallel to their elongation axes suggests that for these crystals shape anisotropy dominates over the effect of interactions with other particles in the chain.

The results presented in Figs. 6–9 show that, in general, in ordered chains that consist of well-aligned, elongated magnetite magnetosomes, the effects of magnetocrystalline and shape anisotropy, as well as magnetic interactions between adjacent particles, reinforce each other to produce a magnetic moment that is strictly parallel to the elongation direction of each crystal and to the chain axis.

### 3.3

#### **Unusually Large Magnetite Magnetosomes, and Scattered or Clustered Crystals**

Unusually large magnetosomes were described from a magnetotactic coccus from the Itaipu Lagoon in Brazil (Farina et al. 1994; Spring et al. 1998). The cells of this organism contain magnetite crystals that are approximately 200 nm in length and thus would not be expected to be in a single-domain magnetic state (Dunlop and Özdemir 1997). Nevertheless, magnetic induction maps obtained from EH measurements by McCartney et al. (2001) reveal that the large magnetite crystals are essentially single magnetic domains, so long as they are in a linear chain configuration (Fig. 10a). The magnetic contour lines fringe out at the edges of the last crystals in the chain, creating flowerlike patterns, but inside the crystals the closely spaced contour lines follow a path that is parallel to the elongation direction of each crystal and to the chain axis. Interestingly, a broken chain configuration results in a more complicated magnetic microstructure, with domain walls and possibly vortex states similar to those reported by Hÿtch et al. (2003) appearing inside the large crystals (Fig. 10b). It therefore appears that for crystals of this size interparticle interactions constrain the direction of the magnetic field and are responsible for the single-domain state of these large magnetite crystals within linear magnetosome chains.

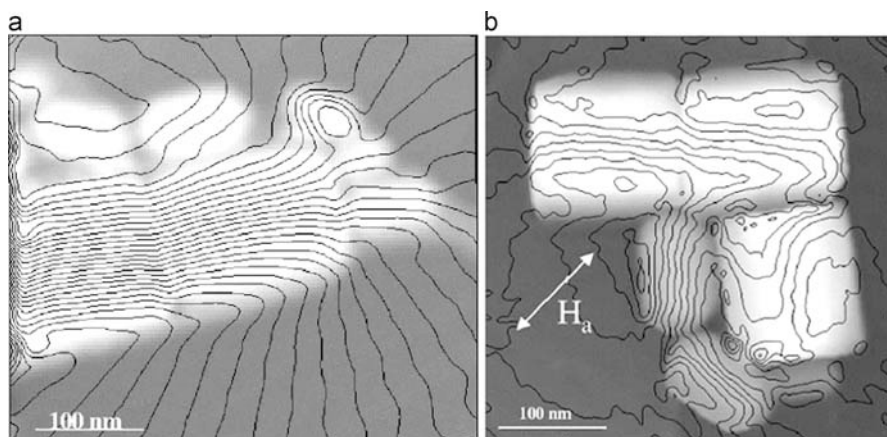


**Fig. 10** Magnetic induction maps recorded using EH from large magnetite magnetosomes from magnetotactic cells that were collected in the Itaipu Lagoon, Brazil. **a** When the large magnetosomes are in a chain configuration, magnetic interactions result in parallel magnetic contour lines within the crystals. Smaller magnetosomes from other types of cells cling to the larger particles. **b** The large magnetosomes are no longer in a single-domain state in broken chains, and exhibit a more complicated magnetic microstructure. The *double-headed arrow* labeled  $H_a$  indicates the direction of the applied magnetic field before recording the remanent magnetic state. The contour spacing is 0.5 rad. (From McCartney et al. 2001)

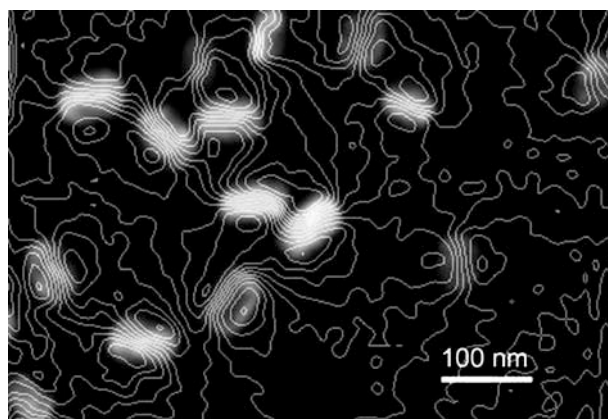


**Fig. 11** Magnetic induction map recorded using EH from scattered magnetite crystals in a single cell of a freshwater coccus. All of the particles are magnetic single domains. The phase contour spacing is 0.125 rad

The profound effect of the orientations and separations of magnetite nanocrystals on their magnetic induction is illustrated by the magnetic induction map shown in Fig. 11. In this freshwater, spherical cell, a disordered



arrangement of prismatic magnetite magnetosomes, which may have resulted in part from air-drying of the cell, results in highly variable directions of the magnetic field inside the crystals. However, as discussed before, in most cases the magnetic contour lines remain parallel to the elongation axis of each crystal, as dictated by shape anisotropy.

## 4

### **The Crystal Structures and Magnetic Properties of Iron Sulfide Magnetosomes**

Iron sulfide magnetosomes contain a larger variety of inorganic phases than iron oxide magnetosomes. Whereas the only magnetosome iron oxide mineral that has been identified is magnetite, the inorganic phase of iron sulfide magnetosomes can comprise either greigite ( $\text{Fe}_3\text{S}_4$ ) (Mann et al. 1990; Farina et al. 1990; Heywood et al. 1990) or mackinawite ( $\text{FeS}$ ) (Pósfai et al. 1998a, b). In addition, a third structure, sphalerite-type cubic  $\text{FeS}$ , was identified tentatively (Pósfai et al. 1998a). It appears that nonmagnetic mackinawite is initially precipitated, before converting into ferrimagnetic greigite. The time that is required for this solid-state phase transition in living cells is unknown, but is presumably within the limits set by the requirement that the majority of the magnetosomes in a cell must always be magnetic. The mackinawite to greigite transition was observed to take place over 10 days in a dehydrated cell on a TEM grid that was stored in air (Pósfai et al. 1998a). The transition may be faster in living cells in their natural sulfide-rich environment.

Mackinawite and greigite have the same cubic-close-packed sulfur substructure. The orientation relationship between mackinawite-like and greigite-like structural elements in crystals that appear to be in a transitional state between the two minerals (Fig. 12) suggests that the conversion of mackinawite takes place with the sulfur substructure remaining intact. Only the iron atoms change their crystallographic positions, one quarter of them being lost from each crystal. The fate of the iron that is released from the magnetosomes remains unknown.

Sulfide magnetosomes typically show heterogeneous, patchy contrast in HRTEM images. This feature likely results from defects that remain in the greigite structure as a result of the solid-state transformation from mackinawite. The greigite structure appears to have nucleated in several places within the crystal shown in Fig. 12. When such greigite nuclei grow and merge, antiphase domain boundaries may remain in the structure. It is also possible that some of the contrast variation seen in HRTEM images is caused by the uneven thickness of the sulfide magnetosomes (Fig. 13b, c). Many greigite magnetosomes appear to be aggregates of several smaller crystals, each in the same crystallographic orientation, producing a single-crystal-like

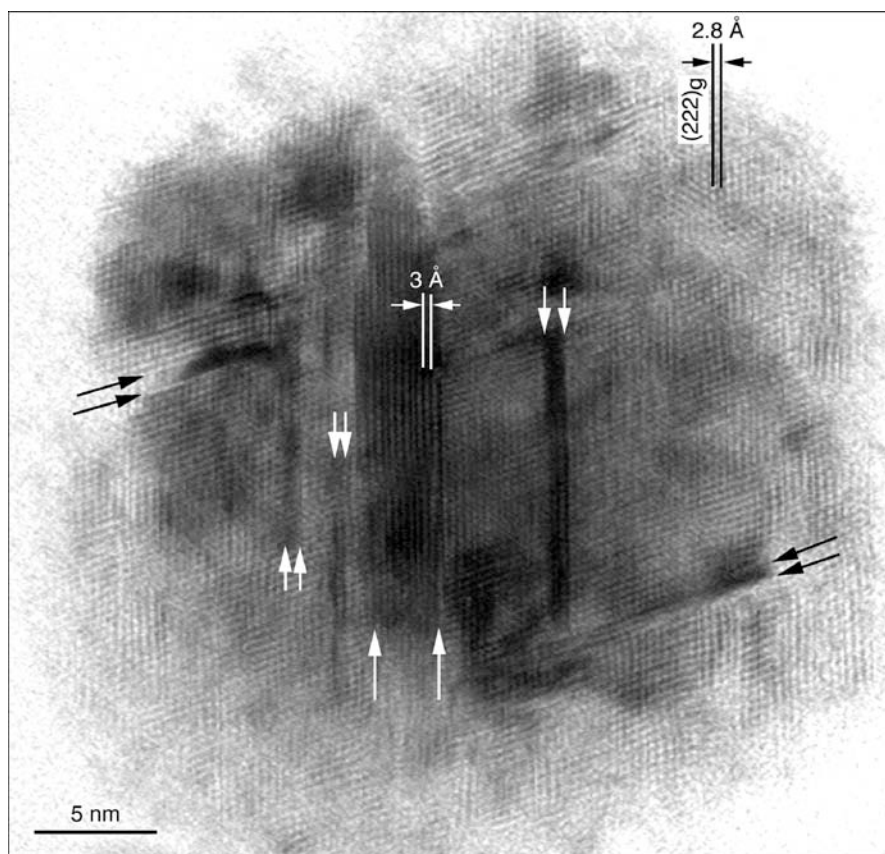


**Fig. 12** HRTEM image of an iron sulfide magnetosome from a multicellular magnetotactic aggregate that contains both mackinawite and greigite structural elements, and is in a transitional state between the two structures. The spacing of lattice fringes in the bands between the *double white arrows* and the *double black arrows* is 3 Å, consistent with  $d(011)$  of mackinawite, whereas in the rest of the crystal the 2.8-Å spacing is consistent with  $d(222)$  of greigite. (From Pósfai et al. 1998a)

aggregate (Kasama et al. 2006a). Interestingly, even though greigite and magnetite are isostructural, spinel-type twins have not been observed in greigite magnetosomes.

Since sulfide-producing magnetotactic bacteria are not yet available in pure culture, and since the number of cells separated magnetically from samples collected from the environment is small, bulk magnetic measurements have not yet been performed on iron sulfide magnetosomes. However, measurements of the magnetic properties of individual sulfide magnetosomes and their chains have recently been performed using EH (Kasama et al. 2006a).

Iron sulfide magnetosomes have been observed both in organisms that are usually referred to as magnetotactic multicellular aggregates or prokaryotes (MMA or MMP) (see also Keim et al., this volume), and in various types of rod-shaped cells (Fig. 13a) (Heywood et al. 1990; Bazylinski et al. 1993; Simmons et al. 2004). In any of these cell types, the sulfide magnetosomes generally form chains that are not as well ordered as is typical in magnetite-bearing organisms. In most studies of sulfide-producing bacteria, the cells were not fixed but left to dry on TEM grids (Mann et al. 1990; Pósfai et al. 1998a, b; Kasama et al. 2006a), raising the concern that some of the disorder in the orientations and positions of the sulfide magnetosomes may be an artifact of the dehydration of the cell. However, even fixed sulfide-producing cells contain fairly disorganized magnetosome chains (Keim et al. 2004), suggesting that the random orientations of the crystallographic and elongation directions of the sulfide magnetosomes within a chain may be typical features of sulfide-producing magnetotactic bacteria.

The disorganized arrangement of sulfide magnetosomes has a strong influence on the magnetic properties of the chain, as illustrated in Fig. 14. This cell is at the point of cell division and contains a multiple chain of magnetosomes that is divided approximately equally between the two daughter cells. Magnetic contour lines derived from EH are superimposed on the image and show that the direction of the magnetic field follows a meandering path along the chain. Highly variable directions of the magnetic moments in individual magnetosomes are apparent in the enlarged inset that shows the central part of the cell and the division plane. Many of the magnetosomes appear

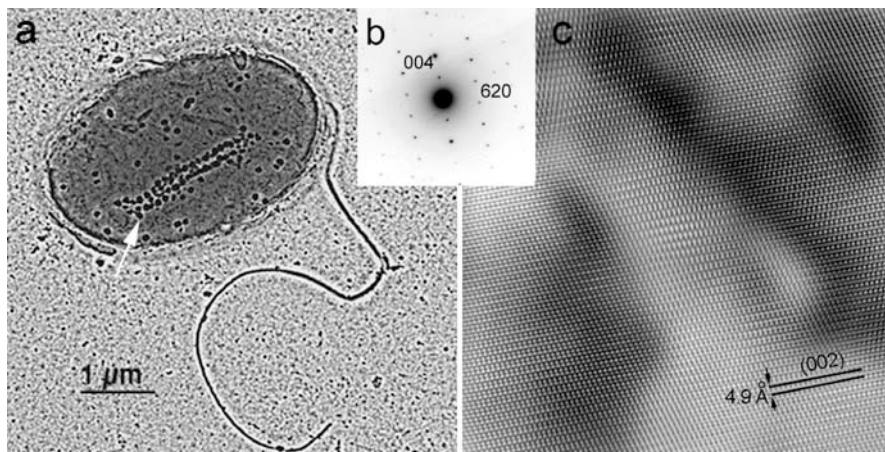


**Fig. 13** **a** Bright-field TEM image of a rod-shaped cell that contains a double chain of iron sulfide magnetosomes. **b** SAED pattern and **c** HRTEM image of the greigite magnetosome marked by an arrow in **a**. The inhomogeneous contrast in **c** is likely caused by variations in the thickness of the crystal. (From Kasama et al. 2006b)

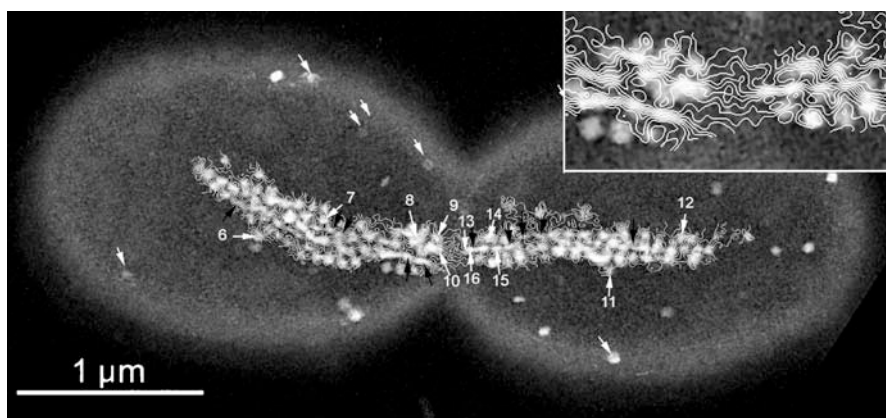


**Fig. 14** Magnetic induction map recorded using EH from a dividing cell that contains iron sulfide magnetosomes. The structures of the numbered crystals were identified and found to be consistent with greigite. The *inset* shows the central part of the cell at higher magnification. The magnetic phase contours are wavy, and their density within individual magnetosomes is highly variable. The *black arrows* mark elongated magnetite crystals. *White arrows without numbers* point to magnetosome-sized, iron-free crystals that contain sulfur and oxygen. The magnetic phase contour spacing is 0.098 rad

to be only weakly magnetic or not magnetic at all. In order to determine whether this magnetic behavior is related to the mineral phase of the sulfide magnetosomes, SAED patterns were obtained from each of the numbered crystals in Fig. 14. Despite the fact that these particles include both apparently strongly and weakly magnetic crystals, all of them were found to be greigite. The apparently nonmagnetic crystals are therefore probably magnetized along a direction that is almost parallel to that of the electron beam. Since EH is sensitive only to the components of the magnetic induction that are perpendicular to the electron beam direction, such crystals may then appear to be nonmagnetic. With regard to magnetotaxis, it is a disadvantage for the cell that its total magnetic moment is reduced by the random orientations of the magnetosomes.

In general, in Fig. 14 the contour lines inside the magnetosomes are parallel to the elongation direction of each crystal. On the basis of SAED patterns obtained from the numbered crystals in Fig. 14, there is no preferred crystallographic direction for the elongation of the sulfide magnetosomes. This observation suggests that magnetocrystalline anisotropy plays little role in determining the direction of elongation of the magnetosomes. The structural defects and the aggregated nature of some of the greigite magnetosomes may affect their magnetic properties. However, as for the magnetite crystals described before, it appears that the magnetic moments of the greigite magnetosomes are influenced most strongly by the shapes and the relative positions of the crystals.

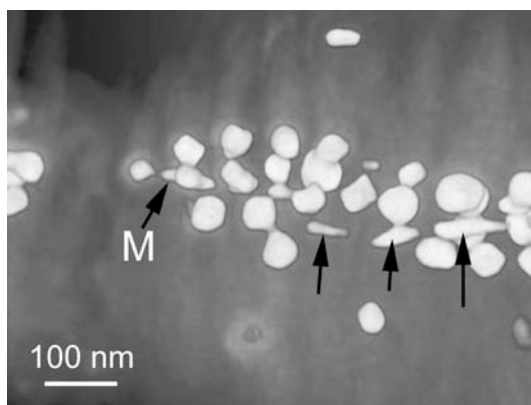


**Fig. 15** Visualization of a three-dimensional electron tomographic reconstruction of the shapes of the magnetosomes within the right half of the boxed region in Fig. 14, derived from a tilt series of high-angle annular dark-field images. The *arrows* mark highly elongated iron oxide crystals. The other magnetosomes are greigite

In addition to the sulfide magnetosomes, magnetite particles occur in the multiple chain shown in Fig. 14. The particles that are marked by dark arrows are highly elongated and contain dense magnetic contours. Quantitative measurements of their magnetic induction (as discussed later), compositional data obtained using energy-filtered images, and an SAED pattern obtained from the particle marked M in Fig. 15 are all consistent with the elongated particles being magnetite. Magnetotactic cells that contained both iron sulfide and iron oxide magnetosomes were described by Bazylinski et al. (1995). In the case of the cell presented in Fig. 14, results from ET (Fig. 15) confirm that the greigite magnetosomes are oriented randomly in the multiple chain, whereas the highly elongated magnetite particles are parallel to the chain axis. The magnetite particles therefore provide the cell with a strongly magnetic “backbone”.

## 5

### Quantitative Measurements Using Electron Holography

Using EH, we can measure the magnetic properties of both individual magnetosomes and entire cells quantitatively. As mentioned before, holographic phase images contain information about both the magnetic induction  $B$  and the MIP  $V_0$  of the sample. In situ magnetization reversal experiments allow the magnetic contribution to the phase shift to be separated from the MIP contribution. If a region of the sample is chosen in which demagnetizing fields are negligible, such as a crystal close to the center of a chain of closely spaced magnetosomes, then the magnetic and MIP contributions to the phase

shift can be used to measure the ratio  $V_0/B$ . The equations that describe the details of this approach are given elsewhere (Simpson et al. 2005).

The ratio  $V_0/B$  was measured experimentally from cells that contained closely spaced prismatic magnetite crystals. The results are plotted in the form of a histogram in Fig. 16. The scatter in the measured values results from the combined effects of noise, diffraction contrast, and residual demagnetizing fields. The magnetic induction can be determined from such measurements of  $V_0/B$  if  $V_0$  is known. Experimentally, the MIP of magnetite has been measured as 17 V (Harrison et al. 2002). Despite the scatter in the measurements shown in Fig. 16, and the possibility of systematic errors, the use of this value for the MIP results in a mean value for the measured magnetic induction of  $0.58 \pm 0.02$  T at room temperature, which is in excellent agreement with the value expected for magnetite (Dunlop and Özdemir 1997). This agreement confirms the chemical purity and magnetic homogeneity of the biogenic crystals.

Quantitative measurements of the magnetic properties of the greigite and magnetite magnetosomes that are visible within the inset in Fig. 14 reveal a relationship between the morphologies, compositions, and magnetic inductions of the magnetosomes in this multiple chain, as shown in Fig. 17. As mentioned before, the sulfide particles in this chain are roughly equidimensional, whereas the oxide particles have elongated shapes. The measured magnetic inductions in the sulfide particles (Fig. 17a) are approximately consistent with values expected from the literature for greigite (approximately 0.16 T) (Dunlop and Özdemir 1997). The magnetic inductions in the elongated oxide particles (Fig. 17b) range from 0.1 to 0.6 T, suggesting that these particles are either magnetite (0.60 T) or maghemite (0.48 T). Since several of the oxide particles show induction values larger than 0.48 T, it is likely that they are magnetite. Many values in Fig. 17 are below the expected 0.16 and 0.60 T for greigite and magnetite, respectively. Several factors may contribute

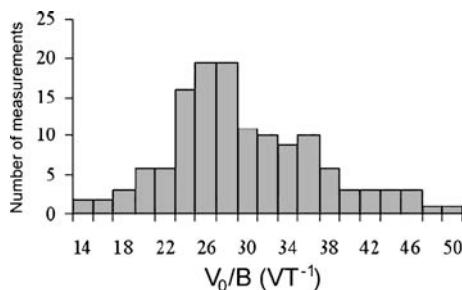


**Fig. 16** The  $V_0/B$  ratio measured from a large number of magnetite magnetosomes in cells that contained two double chains of elongated prismatic crystals (such as the double chain shown in Fig. 6). The mean value of  $V_0/B$  is  $29.5 \pm 0.8$  V T<sup>-1</sup>. (From Simpson et al. 2005)

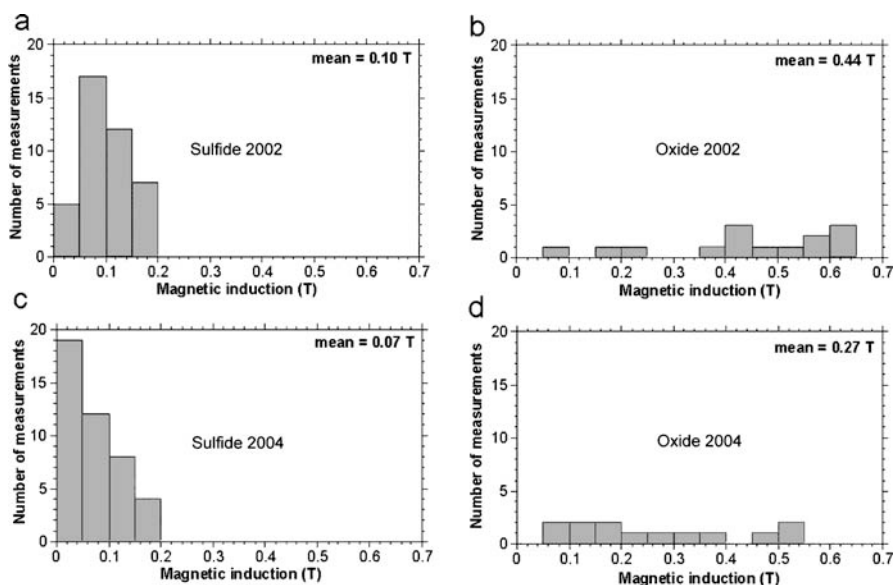


**Fig. 17** The measured magnetic induction of a large number of sulfide and oxide particles in the multiple magnetosome chain shown in Fig. 14, measured both in 2002 and in 2004. Over the 2 years of sample storage, both sulfide and oxide magnetosomes partially oxidized and their magnetic induction decreased. (From Kasama et al. 2006a)

to the apparent reduction in the magnetic induction, including magnetization directions that are not perpendicular to the electron beam direction, the difficulty of measuring the physical dimensions of the nanocrystals precisely, and partial oxidation of the magnetosome minerals. The measurements also provide an opportunity to assess the effects of oxidation of the magnetosomes on their magnetic induction. Figure 17c and d shows that, when the sample was stored in air for 2 years, the magnetic induction of both the sulfide and the oxide magnetosomes decreased.

Using EH, we can measure the magnetic moments of entire cells of magnetotactic bacteria. The procedure, which is described in detail elsewhere (Dunin-Borkowski et al. 2001, 2004), involves measuring the area under the gradient of the magnetic contribution to the phase shift, evaluated in a direction perpendicular to that of the desired magnetic moment. Magnetic moments measured using this approach from single, double, and multiple chains containing cubooctahedral and prismatic magnetite and greigite magnetosomes are listed in Table 1. From Table 1, it is apparent that both the magnetic moment and the magnetic moment per unit length are very similar for all of the chains.

**Table 1** Magnetic moments of individual cells measured using EH

Strain	Magnetosome mineral	Average length of each magnetosome (nm)	Number of magnetosomes in chain	Magnetic moment ( $\text{Am}^2$ )	Length of chain ( $\mu\text{m}$ )	Magnetic moment per unit length ( $\text{Am}^2 \mu\text{m}^{-1}$ )	Reference
MS-1 (Fig. 5)	Magnetite (single chain)	~45	22	$5 \times 10^{-16}$	1.2	$4.2 \times 10^{-16}$	Dunin-Borkowski et al. (1998, 2001)
MV-1 (Fig. 8)	Magnetite (single chain)	~60	15	$7 \times 10^{-16}$	1.6	$4.4 \times 10^{-16}$	Dunin-Borkowski et al. (1998, 2001)
Uncultured coccus (Figs. 6, 7)	Magnetite (double chain)	~80	25	$1.7 \times 10^{-15}$	0.95	$1.8 \times 10^{-15}$	Simpson et al. (2005)
Uncultured, rod-shaped cell (Fig. 13)	Greigite and possibly magnetite (double chain)	~60	57	$9.0 \times 10^{-16}$	2.19	$4.1 \times 10^{-16}$	Kasama et al. (2006a,b)
Uncultured, dividing, rod-shaped cell (Fig. 14)	Greigite and magnetite (multiple chain)	~60 (greigite) ~80 (magnetite)	~155	$1.8 \times 10^{-15}$	2.94	$6.1 \times 10^{-16}$	Kasama et al. (2006a)



## 6

### Summary

In this chapter, the application of HRTEM and off-axis EH to the characterization of the physical and magnetic properties of ferrimagnetic iron oxide and iron sulfide crystals in magnetotactic bacteria has been described. It has been shown that HRTEM images can be used to provide important information about the sizes, shapes, orientations, spatial arrangements, crystal structures, and defect structures of such crystals, and that this information can now be complemented by three-dimensional information about nanoparticle morphologies obtained using the evolving technique of ET. In contrast, off-axis EH can be used to provide quantitative images of the strength and direction of the local magnetic induction, projected in the electron beam direction, inside and outside each crystal, with a spatial resolution of approximately 5 nm. As a result, this technique can be used to assess the magnetic states of individual biogenic crystals both at remanence and during reversal, as well as to measure the strengths of magnetic interactions between neighboring crystals and parameters such as coercivities and magnetic moments.

The results that have been presented in this chapter show that, in general, the ferrimagnetic crystals in magnetite-containing bacteria are crystallographically perfect, morphologically similar to each other, and oriented with their [111] crystallographic axes parallel to the directions of the chains that contain them. Magnetically, the crystals are single domains that are oriented parallel to each other and exhibit little flux leakage. Crystals that are small enough to be superparamagnetic at room temperature or large enough to contain several magnetic domains if they were isolated are constrained to be single domains by magnetostatic interactions with neighboring crystals in the chain. Shape anisotropy appears to be the most important factor controlling the magnetic microstructure of each crystal, followed by interparticle interactions, with magnetocrystalline anisotropy being least important. Similar conclusions are presented for iron sulfide containing cells, the primary difference being the more scattered arrangement of the crystals, resulting in poorer confinement and greater variability in the directions of the field lines in the cell. Significantly, despite the different crystal structures, orientations, arrangements, and magnetic properties of the ferrimagnetic crystals that are formed by different strains of bacteria, EH measurements show that the magnetic moments of different bacterial cells are remarkably consistent with each other, satisfying the requirement for magnetotaxis that a large proportion of the forward motion of each cell should be in the direction of the external magnetic field.

The electron microscopy techniques that have been described here are being developed actively, offering the prospect of improved structural and magnetic information about magnetotactic bacteria in the future. In particular, it may be possible to map both the morphologies and the magnetic vector

fields of entire cells in three dimensions with nanometer spatial resolution by combining EH with ET. In future experiments, it will also be important to optimize sample preparation techniques so that the internal arrangements of cells are always preserved faithfully for electron microscopy.

**Acknowledgements** We thank Ed Simpson and Anna Finlayson for contributions to the EH measurements, and Ryan Chong for ET. This chapter benefited greatly from ongoing collaborations and discussions with Richard Frankel, Dirk Schüler, Dennis Bazylinski, Peter Buseck, and István Dódy. We thank Jian-Min Zuo and Jim Mabon for use of their WebEMAPS HRTEM image simulation software, and Werner Kaminsky for making the WinXMorph crystal morphology software available. R.D.B. acknowledges the Royal Society for support and M.P. acknowledges support from the Hungarian Science Fund (OTKA-T030186).

## References

- Arató B, Szányi Z, Flies C, Schüler D, Frankel RB, Buseck PR, Pósfai M (2005) Crystal-size and shape distributions of magnetite from uncultured magnetotactic bacteria as a potential biomarker. *Am Mineral* 90:1233–1241
- Balkwill DL, Maratea D, Blakemore RP (1980) Ultrastructure of a magnetic spirillum. *J Bacteriol* 141:1399–1408
- Bazylinski DA, Frankel RB (2000) Magnetic iron oxide and iron sulfide minerals within microorganisms. In: Baeuerlein E (ed) *Biomineralization*. Wiley, Weinheim, pp 25–46
- Bazylinski DA, Frankel RB (2004) Magnetosome formation in prokaryotes. *Nat Rev Microbiol* 2:217–230
- Bazylinski DA, Garratt-Reed AJ, Abedi A, Frankel RB (1993) Copper association with iron sulfide magnetosomes in a magnetotactic bacterium. *Arch Microbiol* 160:35–42
- Bazylinski DA, Frankel RB, Heywood BR, Mann S, King JW, Donaghay PL, Hanson AK (1995) Controlled biomineralization of magnetite ( $\text{Fe}_3\text{O}_4$ ) and greigite ( $\text{Fe}_3\text{S}_4$ ) in a magnetotactic bacterium. *Appl Environ Microbiol* 61:3232–3239
- Blakemore RP (1975) Magnetotactic bacteria. *Science* 190:377–379
- Buseck PR, Dunin-Borkowski RE, Devouard B, Frankel RB, McCartney MR, Midgley PA, Pósfai M, Weyland M (2001) Magnetite morphology and life on Mars. *Proc Natl Acad Sci USA* 98:13490–13495
- Clemett SJ, Thomas-Keperta KL, Shimmin J, Morpew M, McIntosh JR, Bazylinski DA, Kirschvink JL, Wentworth SJ, McKay DS, Vali H, Gibson EK, Romanek CS (2002) Crystal morphology of MV-1 magnetite. *Am Mineral* 87:1727–1730
- DeRosier DJ, Klug A (1968) Reconstruction of three dimensional structures from electron micrographs. *Nature* 217:130–134
- Devouard B, Pósfai M, Xin H, Bazylinski DA, Frankel RB, Buseck PR (1998) Magnetite from magnetotactic bacteria: size distributions and twinning. *Am Mineral* 83:1387–1398
- Diaz-Ricci JC, Kirschvink JL (1992) Magnetic domain state and coercivity predictions for biogenic greigite ( $\text{Fe}_3\text{S}_4$ ): a comparison of theory with magnetosome observations. *J Geophys Res* 97:17309–17315
- Dunin-Borkowski RE, McCartney MR, Frankel RB, Bazylinski DA, Pósfai M, Buseck PR (1998) Magnetic microstructure of magnetotactic bacteria by electron holography. *Science* 282:1868–1870

- Dunin-Borkowski RE, McCartney MR, Posfai M, Frankel RB, Bazylinski DA, Buseck PR (2001) Off-axis electron holography of magnetotactic bacteria: magnetic microstructure of strains MV-1 and MS-1. *Eur J Mineral* 13:671–684
- Dunin-Borkowski RE, McCartney MR, Smith DJ (2004) Electron holography of nanostructured materials. In: Nalwa HS (ed) *Encyclopedia of nanoscience and nanotechnology*. American Scientific, pp 41–100
- Dunlop DJ, Özdemir Ö (1997) *Rock magnetism: fundamentals and frontiers*. Cambridge University Press, Cambridge
- Keim CN, Lopes Martins J, Lins de Barros HGP, Lins U, Farina M (2006) The Magnetotactic Multicellular Organism, a multicellular prokaryote from hypersaline environments. In: Schüler D (ed) *Magnetoreception and magnetosomes in bacteria*. Springer, Berlin Heidelberg New York
- Farina M, Esquivel DMS, Lins de Barros HGP (1990) Magnetic iron-sulphur crystals from a magnetotactic microorganism. *Nature* 343:256–258
- Farina M, Kachar B, Lins U, Broderick R, Lins de Barros HGP (1994) The observation of large magnetite crystals from magnetotactic bacteria by electron and atomic force microscopy. *J Microsc* 173:1–8
- Frank J (ed) (1992) *Electron tomography: three-dimensional imaging with the transmission electron microscope*. Springer, Berlin Heidelberg New York
- Frankel RB (1984) Magnetic guidance of organisms. *Annu Rev Biophys Bioeng* 13:85–103
- Golden DC, Ming DW, Morris RV, Brearley A, Lauer HV, Treiman AH, Zolensky ME, Schwandt CS, Lofgren GE, McKay GA (2004) Evidence for exclusively inorganic formation of magnetite in Martian meteorite ALH84001. *Am Mineral* 89:681–695
- Hanzlik M, Winklhofer M, Petersen N (1996) Spatial arrangement of chains of magnetosomes in magnetotactic bacteria. *Earth Planet Sci Lett* 145:125–134
- Harrison RJ, Dunin-Borkowski RE, Putnis A (2002) Direct imaging of nanoscale magnetic interactions in minerals. *Proc Natl Acad Sci USA* 99:16556–16561
- Heywood BR, Bazylinski DA, Garratt-Reed A, Mann S, Frankel RB (1990) Controlled biosynthesis of greigite (Fe<sub>3</sub>S<sub>4</sub>) in magnetotactic bacteria. *Naturwissenschaften* 77:536–538
- Hÿtch MJ, Dunin-Borkowski RE, Scheinfein MR, Moulin J, Duhamel C, Mazaleyra F, Champion Y (2003) Vortex flux channeling in magnetic nanoparticle chains. *Phys Rev Lett* 91:257207
- Iida A, Akai J (1996) TEM study on magnetotactic bacteria and contained magnetite grains as biogenic minerals, mainly from Hokuriku-Niigata region, Japan. *Sci Rep Niigata Univ Ser E* 11:43–66
- Kasama T, Pósfai M, Chong RKK, Finlayson AP, Buseck PR, Frankel RB, Dunin-Borkowski RE (2006a) Magnetic properties, microstructure, composition and morphology of greigite nanocrystals in magnetotactic bacteria from electron holography and tomography. *Am Mineral* 91:1216–1229
- Kasama T, Pósfai M, Chong RKK, Finlayson AP, Dunin-Borkowski RE, Frankel RB (2006b) Magnetic microstructure of iron sulfide crystals in magnetotactic bacteria from off-axis electron holography. *Physica B* (in press)
- Keim CN, Abreu F, Lins U, de Barros HL, Farina M (2004) Cell organization and ultrastructure of a magnetotactic multicellular organism. *J Struct Biol* 145:254–262
- Komeili A (2006) Cell biology and magnetosome protein targeting in MTB. In: Schüler D (ed) *Magnetoreception and magnetosomes in bacteria*. Springer, Berlin Heidelberg New York
- Lins U, McCartney MR, Farina M, Frankel RB, Buseck PR (2005) Habits of magnetosome crystals in coccoid magnetotactic bacteria. *Appl Environ Microbiol* 71:4902–4905

- Mann S, Moench TT, Williams RJP (1984) A high resolution electron microscopic investigation of bacterial magnetite. Implications for crystal growth. *Proc R Soc Lond Ser B* 221:385–393
- Mann S, Sparks NHC, Blakemore RP (1987) Structure, morphology and crystal growth of anisotropic magnetite crystals in magnetotactic bacteria. *Proc R Soc Lond Ser B* 231:477–487
- Mann S, Sparks NHC, Frankel RB, Bazylinski DA, Jannasch HW (1990) Biomineralization of ferrimagnetic greigite (Fe<sub>3</sub>S<sub>4</sub>) and iron pyrite (FeS<sub>2</sub>) in a magnetotactic bacterium. *Nature* 343:258–261
- Matsuda T, Endo J, Osakabe N, Tonomura A (1983) Morphology and structure of biogenic magnetite particles. *Nature* 302:411–412
- McCartney MR, Lins U, Farina M, Buseck PR, Frankel RB (2001) Magnetic microstructure of bacterial magnetite by electron holography. *Eur J Mineral* 13:685–689
- Meldrum FC, Mann S, Heywood BR, Frankel RB, Bazylinski DA (1993a) Electron microscopy study of magnetosomes in a cultured coccoid magnetotactic bacterium. *Proc R Soc Lond Ser B* 251:231–236
- Meldrum FC, Mann S, Heywood BR, Frankel RB, Bazylinski DA (1993b) Electron microscopy study of magnetosomes in two cultured vibrioid magnetotactic bacteria. *Proc R Soc Lond Ser B* 251:237–242
- Midgley PA, Weyland M, Thomas JM, Johnson BFG (2001) Z-contrast tomography: A technique in 3-dimensional nanostructural analysis based on Rutherford scattering. *Chem Commun* 10:907–908
- Moskowitz BM, Frankel RB, Bazylinski DA (1993) Rock magnetic criteria for the detection of biogenic magnetite. *Earth Planet Sci Lett* 120:283–300
- Moskowitz BM, Frankel RB, Bazylinski DA, Jannasch HW, Lovley DR (1989) A comparison of magnetite particles produced anaerobically by magnetotactic and dissimilatory iron-reducing bacteria. *Geophys Res Lett* 16:665–668
- Pósfai M, Buseck PR, Bazylinski DA, Frankel RB (1998a) Reaction sequence of iron sulfide minerals in bacteria and their use as biomarkers. *Science* 280:880–883
- Pósfai M, Buseck PR, Bazylinski DA, Frankel RB (1998b) Iron sulfides from magnetotactic bacteria: Structure, composition, and phase transitions. *Amer Mineral* 83:1469–1481
- Pósfai M, Moskowitz B, Arató B, Schüller D, Flies C, Bazylinski DA, Frankel RB (2006) Properties of intracellular magnetite crystals produced by *Desulfovibrio magneticus* strain RS-1. *Earth Planet Sci Lett* (in press)
- Proksch R, Schäffer TE, Moskowitz BM, Dahlberg ED, Bazylinski DA, Frankel RB (1995) Magnetic force microscopy of the submicron magnetic assembly in a magnetotactic bacterium. *Appl Phys Lett* 66:2582–2584
- Scheffel A, Gruska M, Faivre D, Linaroudis A, Plitzko JM, Schüller D (2005) An acidic protein aligns magnetosomes along a filamentous structure in magnetotactic bacteria. *Nature* 440:110–114
- Simmons SL, Sievert SM, Frankel RB, Bazylinski DA, Edwards KJ (2004) Spatiotemporal distribution of marine magnetotactic bacteria in a seasonally stratified coastal salt pond. *Appl Environ Microbiol* 70:6230–6239
- Simpson ET, Kasama T, Pósfai M, Buseck PR, Harrison RJ, Dunin-Borkowski RE (2005) Magnetic induction mapping of magnetite chains in magnetotactic bacteria at room temperature and close to the Verwey transition using electron holography. *J Phys Conf Ser* 17:108–121

- Sparks NHC, Mann S, Bazylinski DA, Lovley DR, Jannasch HW, Frankel RB (1990) Structure and morphology of magnetite anaerobically-produced by a marine magnetotactic bacterium and a dissimilatory iron-reducing bacterium. *Earth Planet Sci Lett* 98:14–22
- Spring S, Lins U, Amann R, Schleifer K-H, Ferreira LCS, Esquivel DMS, Farina M (1998) Phylogenetic affiliation and ultrastructure of uncultured magnetic bacteria with unusually large magnetosomes. *Arch Microbiol* 169:136–147
- Taylor AP, Barry JC (2004) Magnetosomal matrix: ultrafine structure may template biomineralization of magnetosomes. *J Microsc* 213:180–197
- Taylor AP, Barry JC, Webb RI (2001) Structural and morphological anomalies in magnetosomes: possible biogenic origin for magnetite in ALH84001. *J Microsc* 201:84–106
- Thomas-Keprta KL, Bazylinski DA, Kirschvink JL, Clemett SJ, McKay DS, Wentworth SJ, Vali H, Gibson EK Jr, Romanek CS (2000) Elongated prismatic magnetite crystals in ALH84001 carbonate globules: potential Martian magnetofossils. *Geochim Cosmochim Acta* 64:4049–4081
- Tonomura A (1992) Electron-holographic interference microscopy. *Adv Phys* 41:59–103
- Towe KM, Moench TT (1981) Electron optical characterization of bacterial magnetite. *Earth Planet Sci Lett* 52:213–220
- Vali H, Kirschvink JL (1990) Observation of magnetosome organization, surface structure and iron biomineralization of undescribed magnetic bacteria: Evolutionary speculations. In: Blakemore RP, Frankel RB (eds) *Iron biominerals*. Plenum, New York, pp 97–115
- Völkl E, Allard LF, Joy DC (eds) (1998) *Introduction to electron holography*. Plenum, New York
- Weiss BP, Kim SS, Kirschvink JL, Kopp RE, Sankaran M, Kobayashi A, Komeili A (2004) Ferromagnetic resonance and low-temperature magnetic tests for biogenic magnetite. *Earth Planet Sci Lett* 224:73–89